TUDelft

Delft University of Technology

On-site aerodynamics investigation of speed skating

Spoelstra, Alexander; Terra, Wouter; Sciacchitano, Andrea

On-site aerodynamics investigation of speed skating

Alexander Spoelstra [a], Wouter Terra [b], Andrea Sciacchitano [a,*]

[a] *Aerospace Engineering Department, Delft University of Technology, Delft, the Netherlands*
[b] *TeamNL Experts, NOC*NSF, Arnhem, the Netherlands*

A B S T R A C T

An aerodynamic assessment is presented of two elite skaters, each in two different skating postures, at the ice-rink Thialf in Heerenveen, the Netherlands, via on-site Ring of Fire (RoF) measurements. This experimental approach adopts stereoscopic Particle Image Velocimetry (Stereo-PIV) to measure the flow upstream and downstream of the skaters. Both skaters transit through the RoF 20 times, 10 in each skating configurations. Athlete A skates with two hands on the back and with one arm on the back and one loose. Athlete B skates with one arm loose in a normal deep sit and in an extreme deep sit. All tests are performed at a nominal skating speed of 11 m/s.

Firstly, the wake velocity fields of skater A with two hands on the back are presented throughout five different phases of the skate stroke. Significant variations in the distribution of the velocity deficit downstream of the athlete are observed, which suggest corresponding variations in the skater's aerodynamic drag. These velocity fields are also compared to literature and the similarities and differences are discussed between the flow around a static skater and that in the natural skating motion. Secondly, average streamwise velocity and vorticity fields for all 4 different postures are presented and compared. It is observed that for all cases the maximum velocity deficit in the wake is in the range of $0.45 \leq u_x^* \leq 0.55$ and is located behind the lower back and upper legs. Furthermore, a characteristic vortex pair is observed downstream of the skater's hips for all four skating configurations, indicating it is independent of the athlete, the posture, and skating phase.

The ensemble average aerodynamic drag is evaluated via a control volume approach along the wake behind the skater, accounting for the non-uniform flow conditions prior to the skater's passage. The uncertainty of the average drag measurements from the present RoF is about 5%. The results show that the optimization of the deep sit, e.g. the trunk and knee angle, yields a reduction by 7.5% of the skater's aerodynamic drag. Conversely, the difference in drag between two arms loose and one arm loose is not statistically significant.

1. Introduction

The aerodynamic drag plays a crucial role in elite speed skating performance. Oggiano and Sætran (2010) estimated the contribution of the aerodynamic drag, or air resistance, to about 90% of the overall force opposing the skater's motion. Knowing that the speed of a skater depends on the balance between the propelling forces (generated by the athlete) and the opposing forces, reducing the main opposing force yields an increase of the skater's speed and in turn of the chances of winning races.

The aerodynamic drag of an individual skater can be reduced, among others, by streamlining the athlete's garments (van Ingen Schenau, 1982; Oggiano and Sætran, 2008; Brownlie and Kyle, 2012; Chowdhury et al., 2015; Timmer and Veldhuis, 2021; Puelles Magán et al., 2021) and changing the athlete's posture, e.g. optimizing the trunk or knee angle (van Ingen Schenau, 1982). To the best knowledge of the authors, all these aerodynamic studies have considered skaters, or skater models, in static poses in wind tunnels or numerical simulations in order to measure differences in drag. Skating, however, is a very dynamic sport in

which the posture of the athlete continuously changes through a repetitive motion of skate strokes (e.g. Van der Kruk, 2018). Such changing posture also affects the aerodynamic drag (D'Auteuil et al., 2012); hence, when aiming at reducing the aerodynamic drag of a skater, the entire skating stroke should be considered, instead of a single pose only. Such an aerodynamic assessment of a skater during the natural skating motion is missing in the literature, presumably because of the associated challenges.

In other speed sports such as cycling, field testing or on-site aerodynamic testing has been successfully achieved. The most common approach relies on the use of power meters: the cycling speed and the power exerted by the athlete on the bike are measured to estimate the aerodynamic drag acting on the cyclist (e.g. Broker et al., 1999). In ice-skating, instrumented clap skates can measure the power exerted to the ice. However, in contrast to cycling, the relation between the exerted power and the forward motion is yet unknown (Van der Kruk, 2018), thus hindering the evaluation of the aerodynamic drag. An alternative to power meter measurements is the application of the Ring-of-Fire system, where the aerodynamic drag of a transiting object is determined based

---

* Corresponding author.
E-mail address: a.sciacchitano@tudelft.nl (A. Sciacchitano).

on air flow measurements around the object and the application of the conservation of momentum. This measurement system has been validated for aerodynamic investigation of elite cyclists (Spoelstra et al., 2019, 2020) and seems a promising tool for the study of in-field skating aerodynamics.

Based on the above, this work aims at assessing the aerodynamic performance of speed skaters during their natural skating motion by Ring of Fire measurements. Velocity and vorticity fields downstream of two elite skaters are presented throughout the different phases of the skate stroke, thus providing a better understanding of the overall skating aerodynamics. The velocity fields are also compared to literature and the similarities and differences are discussed between the flow around a static skater and one in his or her natural motion. Furthermore, for each of the skaters, two different skating configurations are investigated, namely skating with one arm vs two arms on the back and low trunk vs high trunk. Finally, the aerodynamic drag is presented of the different skating configurations.

2. Drag evaluation by momentum analysis

The works of Spoelstra et al. (2019) and Terra et al. (2017) have established the principles of drag evaluation for transiting objects through the Ring of Fire concept. By invoking the conservation of momentum in a control volume containing the athlete and moving with him or her, the instantaneous drag force $D(t)$ can be evaluated. It is assumed that the athlete moves at a constant speed u_A relative to the fixed reference frame of the ice rink. The motion of air prior to the skater's passage is expressed as u_1. After the passage, the air is accelerated in the same direction as the skater, whose wake features a velocity field denoted as u_2. This is illustrated in Fig. 1. When expressing velocity and momentum in the skaters' frame of reference, the following expression returns the instantaneous drag:

$$D(t) = \underbrace{\rho \iint_{S_1} (u_1 - u_A)^2 dS - \rho \iint_{S_2} (u_2 - u_A)^2 dS}_{\text{Momentum term}} + \underbrace{\iint_{S_1} p_1 dS - \iint_{S_2} p_2 dS}_{\text{Pressure term}} \tag{1}$$

where ρ is the air density and p is the static pressure. The mass flow over surfaces S_1 and S_2 (prior and after the athlete's passage, respectively) must be preserved for this equation to be valid. This methodology measures the drag force in the X-direction (lane direction), whereas the skater experiences a force in the direction opposite to their motion, which is generally not parallel to the skating lanes. Considering the typical angles of the skating path with respect to the lanes of the ice rink (maximum $\pm 20°$), the drag may be underestimated by up to 6%.
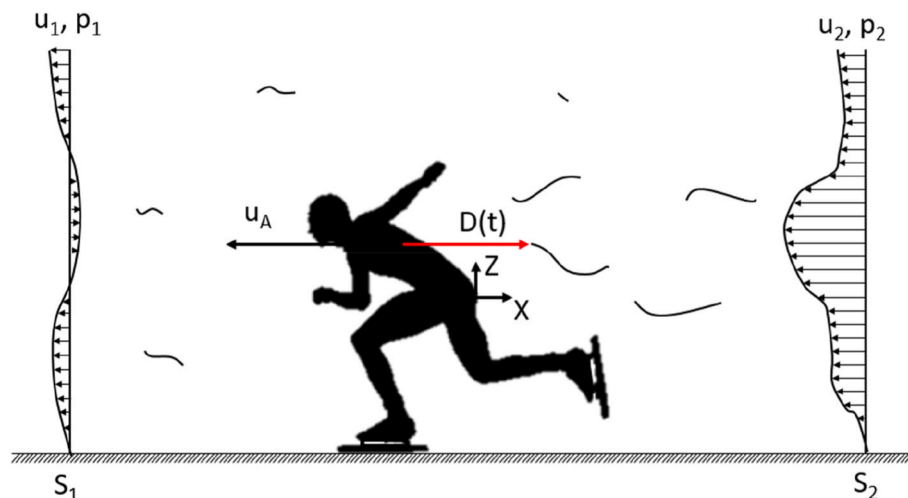
However, considering that the skating path does not vary among the different configurations investigated, this work is able to assess the drag differences among different skating configurations.

Previous studies have indicated that the unsteady flow behavior in the wake of bluff objects yields large uncertainties when the aerodynamic drag is evaluated from a single passage via the Ring of Fire approach (Terra et al., 2017; Spoelstra et al., 2019). To achieve statistical convergence of the drag estimate, averaging from numerous passages is performed in two steps. Firstly, the average drag in time from multiple passages ($\overline{D}_{\text{multi}}(t)$) is determined:

$$\overline{D}_{\text{multi}}(t) = \frac{1}{M} \sum_{i=1}^{M} D_i(t) \tag{2}$$

where M is the total number of passages. Secondly, time averaging is performed over every single time instant in the wake to determine the final ensemble-average $\overline{D}_{ens}$:

$$\overline{D}_{\text{ens}} = \frac{1}{N} \sum_{j=1}^{N} \overline{D}_{\text{multi}}(t_j) \tag{3}$$

where N is the number of time instants composing the measurement. As customary in sports aerodynamics investigation (see for instance Crouch et al., 2014), the drag results are expressed in terms of drag area C_dA, whereby the latter is obtained by dividing the measured drag force by the flow dynamic pressure evaluated in a frame of reference moving with the athlete.

3. Experimental setup and procedures

3.1. Test facility and subjects

The measurements were conducted at Thialf, an ice arena in Heerenveen (the Netherlands) used for long track speed skating, short track speed skating, ice hockey, and figure skating (Thialf, 2021). Experiments were conducted on the 400 m track (see Figs. 2 and 3). A male and a female skaters, both professional athletes, participated in the experiment. To keep their identities anonymous, we only report their approximate anthropomorphic characteristics. Their body masses were in the range of 75–80 kg and 65–70 kg, and their heights were in the range of 175–180 cm and 170–175 cm for the male and female athlete, respectively. Their shoulder widths were approximately 50 cm. They wore a typical long leg and long arm hooded skate suit. In addition to the skin suit, the skaters wore laser safety goggles for protection against the PIV laser light. During the entire measurement campaign, the air
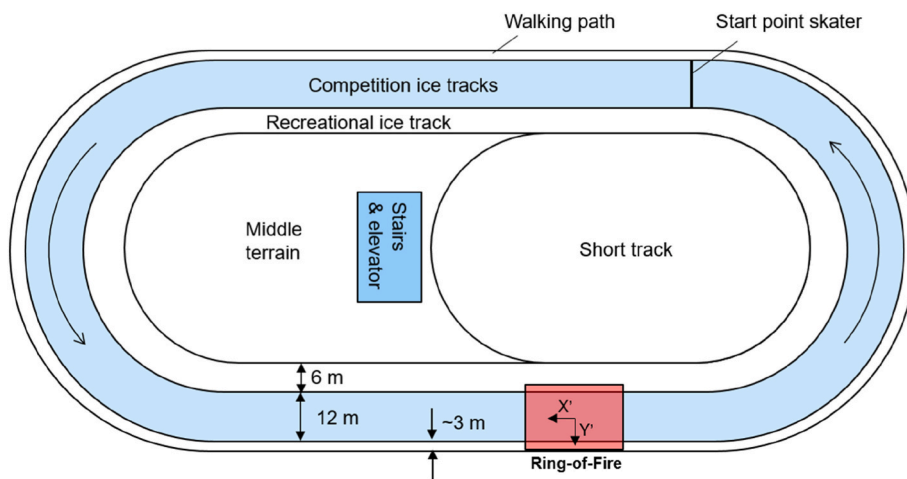

Fig. 1. Schematic view of the velocity distribution before and after the passage of the skater in the fixed reference frame of the ice rink.

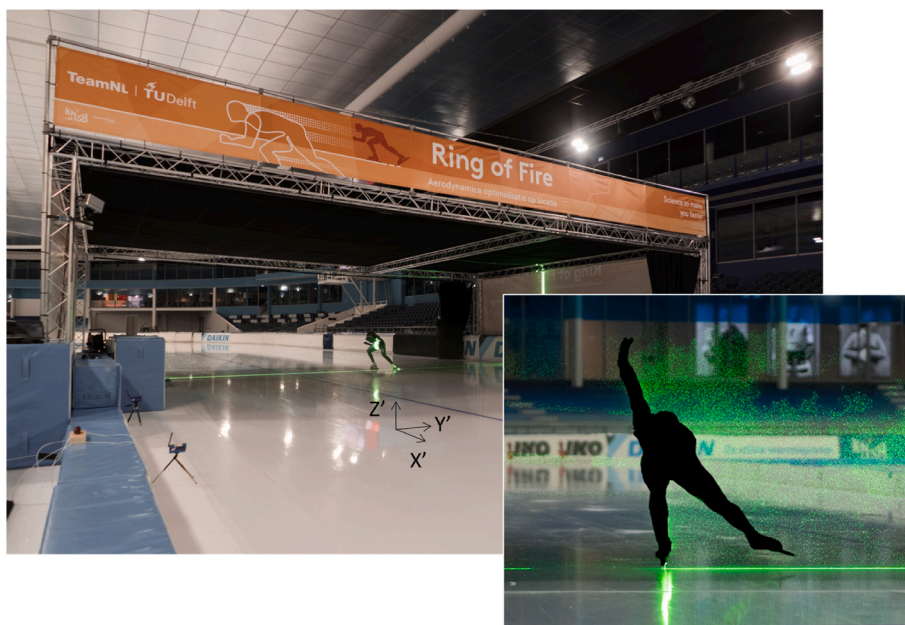**Fig. 2.** Schematic top view of the testing facility.

Fig. 3. Ring of Fire on the ice of Thialf. An athlete skating through a cloud of helium filled soap bubbles illuminated by laser light.

ventilation system of Thialf was shut off so to minimize any air circulation.

For each of the participants, two different skating configurations were examined. The configurations were characterized by the position of the arms (loose vs. stuck to the body) and the knee θ_0 and trunk θ_1 angles (Fig. 4), both evaluated at skating phase 3 (see section 3.4 for the description of the skating phases). For the female participant, skating with two arms on the back vs. one arm on the back and one loose was investigated for the body angles $\theta_0 = 97^o$ and $\theta_1 = 16^o$. The male participant, instead, skated all the time with one arm loose changing his body angles between a high trunk posture ($\theta_0 = 92^o$ and $\theta_1 = 16^o$) and a low trunk posture ($\theta_0 = 84^o$ and $\theta_1 = 7^o$). The uncertainty of the body angles is estimated at 3°. A summary of the different body angles is given in Table 1 and a frontal and side view of each of the postures is shown in Fig. 4.

Two right-handed coordinate systems are introduced. The system of reference that moves with the athlete is denoted with (X,Y,Z) and has its origin at the rearmost point of the back of the athlete (Figs. 1 and 7). A stationary system of coordinate (X′,Y′,Z′), with the origin on the ground at the laser sheet location, is used to represent the skaters' positions

along the track and the measurement location (Figs. 2 and 3).

3.2. PIV system

The velocity distribution upstream and in the wake of the skater was obtained by large-scale stereoscopic-PIV. The use of neutrally buoyant helium-filled soap bubbles (HFSB) as flow tracers (Scarano et al., 2015), with an average diameter between 0.3 and 0.4 mm, provided sufficient light scattering to visualize the flow in a field of view of approximately 10 m^2. A tunnel of $10 \times 13 \times 3$ m^3 in X′, Y′, and Z′ directions (see Fig. 3) was used to confine the bubbles within the measurement volume. The tunnel had an open inlet and outlet to allow the skater to transit and was equipped with optical access on one side for illumination purposes. The HFSB were introduced into the tunnel by an in-house seeding system integrating 200 bubble generators, located 1 m upstream of the measurement plane and on the warm-up lane of the ice track (Fig. 5). A dual-cavity Quantronix Darwin Duo Nd:YLF laser (pulse energy of 2×25 mJ at frequency of 1 kHz, 527 nm wavelength) provided pulsed illumination. The laser beam was shaped into a 50 mm thick sheet by means of laser optics. The field of view was imaged by two Photron Fast
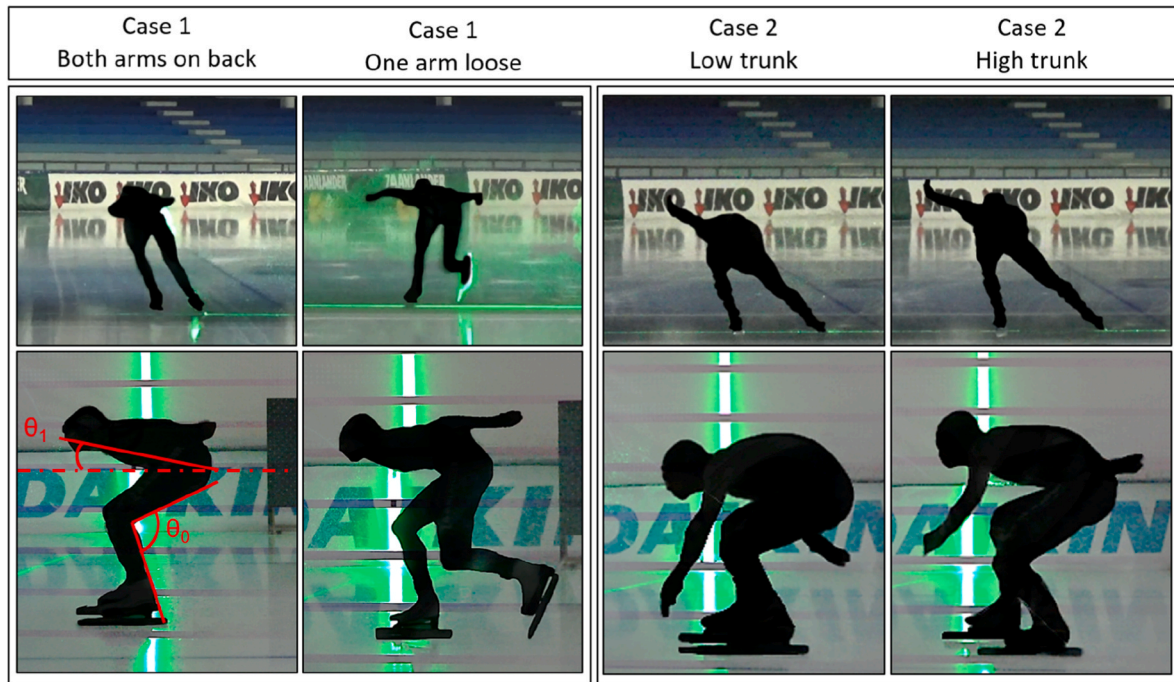
Fig. 4. Frontal and side views of the four different postures studied in this work.

Table 1

Summary of the body angle for the different postures studied in this work.

Case 1		Case 2	
Both arms on back	One arm loose	Low trunk	High trunk
$\theta_0 = 97°$	$\theta_0 = 97°$	$\theta_0 = 84°$	$\theta_0 = 92°$
$\theta_1 = 16°$	$\theta_1 = 16°$	$\theta_1 = 7°$	$\theta_1 = 16°$

CAM SA1 cameras (CMOS, 1024×1024 pixels, 20 μm pixel pitch, 12 bits) equipped with 50 mm objectives at f/5.6; the sensor size was cropped to 1024×752 pixels to record only the flow region illuminated by the laser. The cameras were mounted onto the metal structure of the tunnel 6 m upstream of the measurement plane at a height of 2.5 m, with an angular separation of 90°, imaging a field of view of $4 \times 2.9 \, m^2$. The resulting magnification factor was 0.005 and the digital image resolution 0.26 px/mm. A detailed sketch of the RoF setup is shown in Fig. 5.

3.3. Measurement procedure

The PIV system was calibrated at the beginning of each measurement day. Bubble production was initiated about 2 min before the start of each run to achieve a uniform tracer distribution with sufficient concentration in the measurement domain. The tracer particles were held in the measurement domain by closing entrance and exit gates of the tunnel before the passage of the skater. The soap reservoir was heated using lamps so to guarantee the stable production of the HFSB tracers at the low temperatures in the arena (approximately 10 °C). For each posture, the measurements were repeated 10 times to build an ensemble average estimate of the aerodynamic drag. For all trials, the athlete started on the opposite side of the track (marked in Fig. 2), accelerated to the prescribed velocity of 11 m/s and maintained such velocity until the corner after the measurement region. Considering that the kinematic viscosity of air at 10 °C is $\nu = 1.43 \cdot 10^{-5} \, m^2/s$, the resulting Reynolds number is $Re_c \approx 3.8 \cdot 10^5$ based on the shoulder width $c = 50$ cm.

PIV image acquisition was conducted at 0.5 kHz. Sets of 1000 consecutive image pairs were stored starting from 1 s prior to the passage of the skater, and ending 1 s after the passage. The velocity and
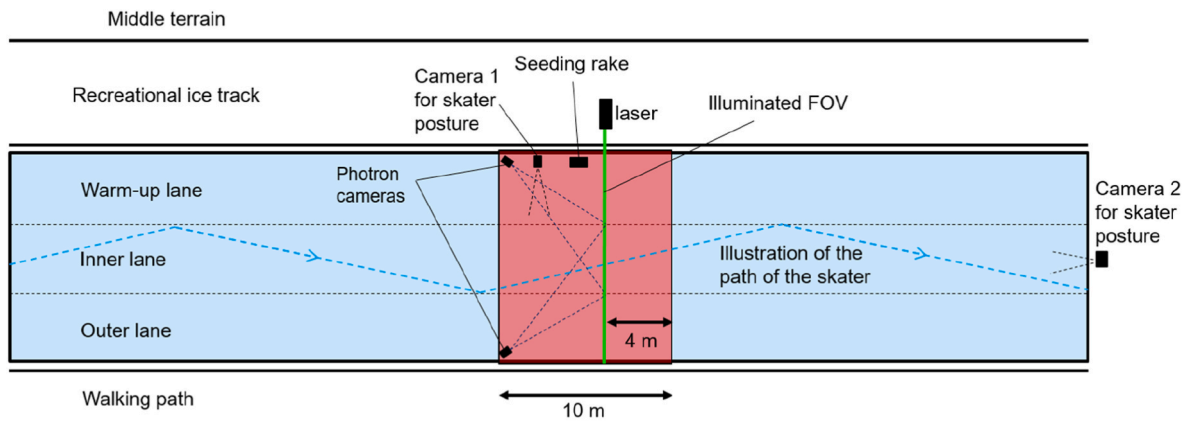

Fig. 5. Schematic representation of the experimental layout of the Ring of Fire.

position of the skater when skating through the Ring of Fire setup were monitored with the ProChip Timing System by MYLAPS Sports Timing (MYLAPS, 2021) and two extra cameras, respectively (see Fig. 5). One of the cameras provided a side view of the skater and the other a frontal view. Images taken by these cameras can be seen in Fig. 4.

3.4. Skating phases

During the experiments, the skaters were not instructed to pass through the measurement plane in a specific phase of the skating motion; hence, the pose of the skater passing through the measurement plane varied between repeating passages through the Ring of Fire system. All skater poses are categorized into one out of five phases of the skating motion, which are described by van der Kruk et al. (2018) and shown in Fig. 6. Phase 1 is the glide phase, during which the mass of the skater is supported over one leg while both skates are on the ice. The second phase, also known as the push-off phase, starts when the skater moves his center of mass away from the support leg, thus introducing a leg extension. The push-off phase ends when the leg is at its maximal extension. In phase 3, the extended leg leaves the ice, while in phase 4 it is retracted under the body of the skater. Phase 4 ends when the skate is placed on the ice again, after which the glide phase (phase 5) begins again thus completing one stroke. This categorization is used later in this work to discuss the variation of the skater's near wake during the skating motion.

3.5. Data reduction

The focus of this work is determining the flow fields along the skaters' wakes and evaluating the aerodynamic drag. Given the relatively high acquisition frequency (0.5 kHz) and the velocity of the skaters (11 m/s), processing the entire set of images would result in a measurement every 2 cm of motion of the skater, which is considered an unnecessarily high sampling rate. Therefore, the acquired PIV images of the wake flow fields are down-sampled such that only 10 image pairs with a spacing of 50 images between pairs are processed. The first image pair is chosen directly after the skater passes through the laser sheet. In other words, in the wake of the skater ten velocity fields are processed with a 0.1 s interval, in which approximately 1 m is covered by the skater. The down-sampling process for the first four velocity fields is illustrated in Fig. 7. The velocity field closest to the athlete is later used in this work to discuss the skater's near wake. The remaining ones are used only for drag determination, where the number of wake velocity fields corresponds to the number N of time instants composing the measurement (see Equation (3)).

The chosen image pairs are processed by cross-correlation analysis using the LaVision DaVis 8.4 software. Following Spoelstra et al. (2020), the final interrogation window size is selected to be 32×32 pixels (100×100 mm^2), and the overlap factor is set to 75%. Before the passage of the skater, the flow velocity is expected to be very low (well below 1 m/s), thus resulting in sub-pixel particle image displacements. Hence, to increase the precision of the environment flow velocity measurements, image pairs are considered with a time separation of 2 ms, or ten times the time separation associated with the acquisition frequency, which then result in particle image displacements of several pixels.

The evaluation of the skater's drag via the control volume approach requires that mass conservation at the inflow and outflow of the domain is accurately satisfied, assuming there is no momentum transfer through the side faces of the domain. However, since the velocity along the side of the measurement domain is unknown, this assumption cannot be made in the current measurement. One way to mitigate the errors associated with an approximate conservation of mass is to reduce the momentum analysis to the area where the largest deficit occurs. This is done by the wake contouring method discussed in Spoelstra et al. (2020). Furthermore, the pressure field is reconstructed by solving the pressure Poisson equation (PPE) (van Oudheusden, 2013). Neumann boundary conditions are applied at the boundaries and the resulting pressure distribution is scaled with the measured quiescent air pressure as reference.

The ensemble average drag area (Equation (3)) is computed for each skating posture. The final number of passages used for ensemble averaging (after discarding the faulty ones characterized by uneven seeding distribution) varies for each case from 8 to 10. For the drag evaluation, the first velocity field, at 0.1 m behind the skater, of each skater passage is discarded because of reflections in the PIV images in some of the measurements.

Following Spoelstra et al. (2019), the streamwise velocity and vorticity in the wake of the skater in the (X,Y,Z) frame of reference are made dimensionless with the velocity of the athlete u_A and their characteristic length scale c and reads as:

$$u_x^* = \frac{u_2 - u_A}{|u_A|} \tag{4}$$

$$\omega_x^* = \frac{\omega_2 c}{|u_A|} \tag{5}$$

The approximate shoulder width $c = 50$ cm is chosen as the characteristic length scale. Notice that both u_A and u_2 are typically negative (with $|u_A|$ typically larger than $|u_2|$), because the skater moves along the negative X' direction. The dimensionless streamwise velocity u_x^* is rewritten in the frame of reference of the skater, meaning that when $u_x^* = 0$, the velocity deficit equals the skater velocity, and when $u_x^* = 1$ there is no velocity deficit behind the skater.

4. Results

4.1. Environmental airflow conditions before transit

The environmental air conditions experienced by the skaters can have a significant effect on the skaters' aerodynamic drag (D'Auteuil et al., 2012). Therefore, the air flow before the passage of the skater is characterized, which rarely is completely still. External conditions as well as the seeding injection cause the environmental flow motions to
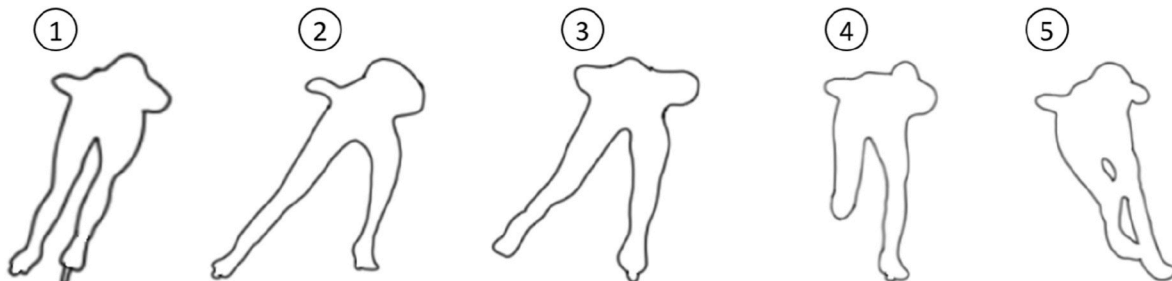

Fig. 6. Contours of the skater (configuration: two hands on the back) in the five phases during the skating motion as introduced by van der Kruk et al. (2018). The skater contours have been obtained from the present experiments.
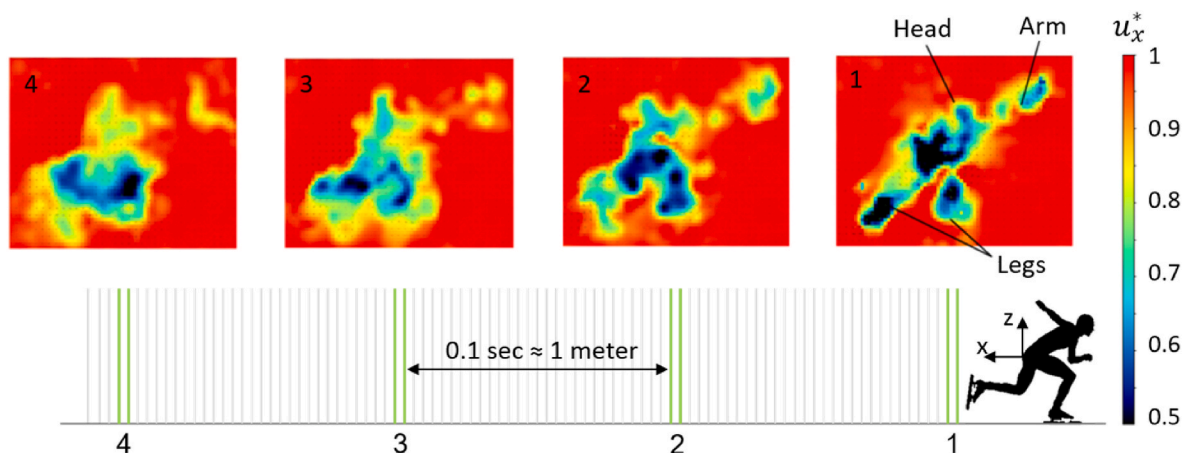
Fig. 7. Example of velocity fields measured with the Ring of Fire for each passage of a skater. Grey are all acquired images, green are the ones processed for analysis of the wake flow and drag determination.

have a velocity that is generally non-zero, non-uniform, and non-stationary. The time average environmental flow field and the RMS of the velocity fluctuations are depicted in Figs. 8 and 9, respectively. These statistics are obtained by analyzing the flow fields 1 s before 20 passages of the skaters.

The seeding injection from the left (negative Y' values) creates a clear inflow of momentum into the measurement region. Higher velocities up to 0.15 m/s for the streamwise and vertical velocity components, and exceeding 0.20 m/s for the horizontal velocity component, are observed on the top side of the domain; conversely, in the rest of the measurement region, all the velocity components are within ± 0.05 m/s. Based on linear error propagation (Sciacchitano and Wieneke, 2016), considering 20 independent samples per case (number of individual runs), the standard uncertainty of the free-stream measurements is about 0.02 m/s.

Also in terms of fluctuations (Fig. 9), the top-left side is clearly influenced by the seeding injection with peaks in RMS exceeding 0.10 m/s for the streamwise and vertical velocity components and up to 0.16 m/s for the horizontal velocity component. On the bottom side, instead, the RMS values typically remain below 0.05 m/s. In almost all runs, the skaters passed through the measurement region at $-1 \text{ m} \leq Y' \leq 1 \text{ m}$ and

hence, for a correct estimate of the drag value, the velocity distribution prior to the passage is taken into account for the drag computation via equation (1), because it contributes to the overall momentum budget, as also discussed by Terra et al. (2018).

4.2. Flow visualizations at the different skating phases

In this section, the skater's near wake velocity is presented approximately 50 cm downstream of the athletes' thighs (plane one in Fig. 7). For sake of conciseness, only one of the four skating configurations is considered here, providing a general understanding of the variations of the wake during the skating motion. The next section focuses on the differences and similarities in the wake flow fields between configurations. Fig. 10 presents the streamwise velocity in the wake together with the corresponding skating phase. Note that the skater contours in Fig. 10 are meant as an indication of the skater's position with respect to the wake and do not reproduce the exact location of the skater. From the instantaneous velocity fields (snapshots of a single skater passage), it is observed that the wake is clearly changing throughout the skating motion. In phase 1, with both skates on the ice and the legs relatively close together, areas of significant velocity deficit are observed downstream of
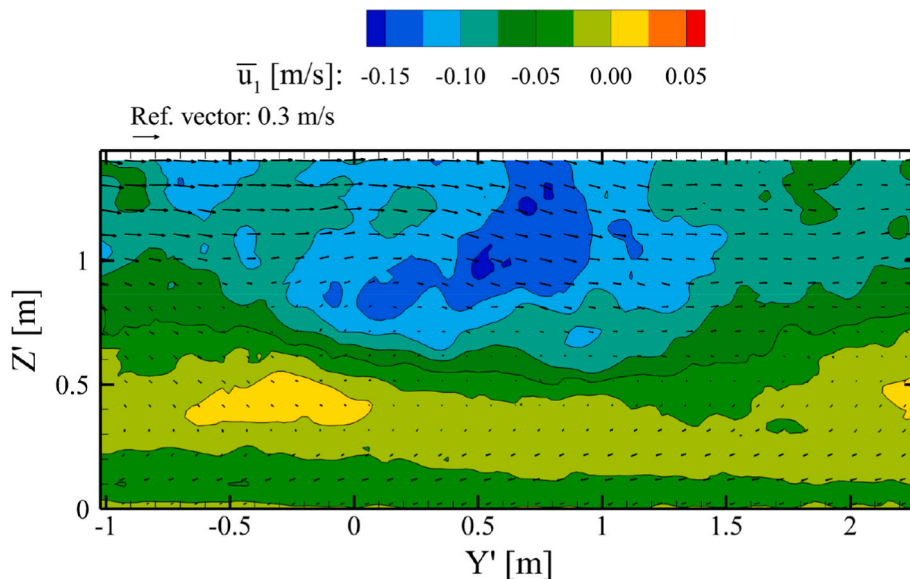

Fig. 8. The environmental flow field 1 s before the passage of the athlete averaged over 0.1 s and 20 runs ($20 \times 0.1s$). Velocity vectors and colour contours represent the in-plane velocity components and the streamwise velocity component, respectively.
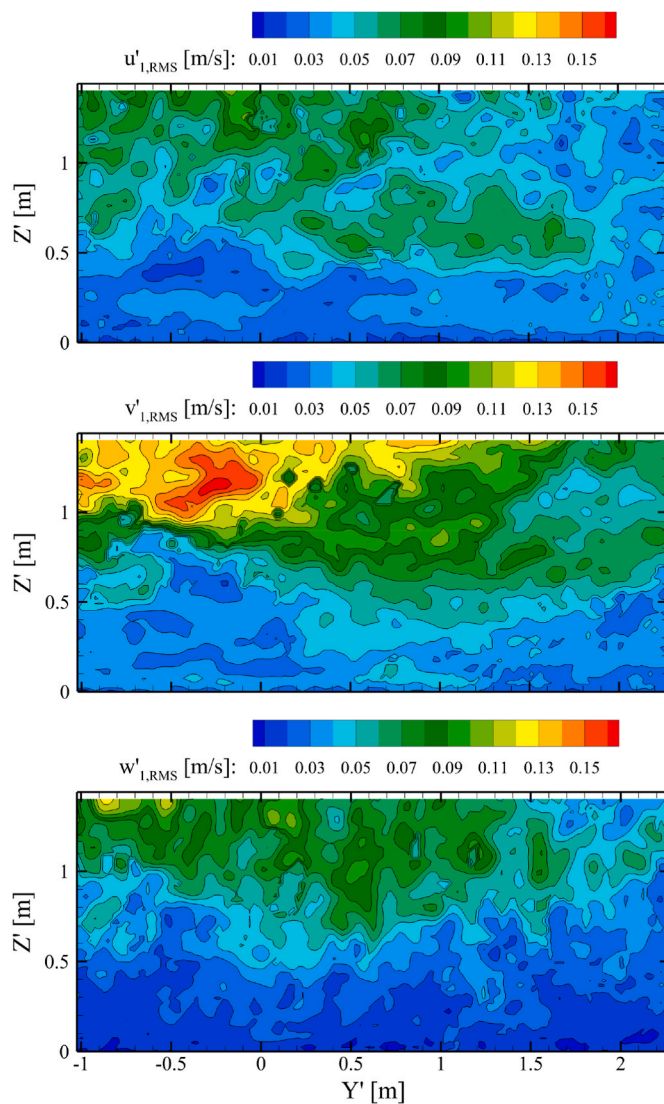
Fig. 9. RMS of the velocity fluctuations in the streamwise (top), horizontal (middle) and vertical (bottom) directions 1 s before the passage of the athlete averaged over 0.1 s and 20 runs (20 × 0.1s).

the legs and the upper body. The wakes of the left and the right legs have already merged, suggesting that their interaction occurs in the first 50 cm from the skater. In phase 2, instead, the legs are further apart and the wakes of the lower legs and feet are clearly observed as individual flow structures. In this phase, the wake is relatively large, hinting to a high value of the aerodynamic drag, which will be discussed further at the end of this section. When moving to phase 3, the skater lifts the left leg and retracts it. Hence, the wake of the left leg moves closer to that of the right leg, and the longitudinal velocity deficit reduces. In skating phase 4, the legs are brought closer together and, as a consequence, their wakes merge again and the peak velocity deficit increases. Finally, in phase 5, when the skater is leaning to the left, the wake is further narrowed and the velocity deficit behind the legs peaks. When comparing the velocity distributions of the different skating phases, it is also observed that the vertical extension of the wake increases from phase 1 to 3, and subsequently decreases through phase 4 and 5. This variation in wake height is ascribed to the up-and-down movement of the skater's upper body, as reported by van der Kruk et al. (2018).

A reliable estimation of the aerodynamic drag of each of the skating phases requires a substantial ensemble of velocity snapshots in each phase. From the present data set, only one or a few near-wake flow fields

per phase are available; hence, an accurate estimation of the variation of the aerodynamic drag is not possible. Instead, drag data from literature is used to relate to the present velocity fields. D'Auteuil et al. (2012) measured the aerodynamic drag on a static skater mannequin in three different poses, which may be categorized as phases 2, 4 and 5. In phase 2, the aerodynamic drag peaks, while it is minimum in phase 4. This corresponds to the relatively widespread and compact wakes in phase 2 and 4, respectively, resulting from the different leg orientations. Additional measurements on skaters on the ice would be necessary for a more detailed discussion on the relation between the variation of the wake velocity and the aerodynamic drag throughout the skating motion.

4.3. Flow visualizations for skater A (Case 1): two arms vs. one arm on the back

The average velocity and vorticity fields measured 0.5 m behind the lower back of the skater for both configurations in case 1 are shown in Figs. 11 and 12, respectively. For both configurations, the average is obtained from 2 passages when the skater is in phase 4.

The streamwise velocity contours show clear differences, thus indicating a strong dependence on the skating posture. The wake of the athlete with both arms on the back, Fig. 11-left, exhibits two distinct regions of high velocity deficit. The highest deficit (lowest u_x^*) is located behind the lower back (Z = 0.6 m & Y = 0 m), whereas the second region of deficit is located behind the legs (Z = 0.3 & Y = −0.4 m). Instead, in the configuration with only one arm on the back (Fig. 11-right), the wakes of the two legs appear to be separated, rather than merged as in the other posture; this result is attributed to the fact that the skater had her leg further apart. The strongest velocity deficit occurs behind the left leg (Z = 0.5 m & Y = 0 m), which is deflected downstream. Additionally, the arm that is loose, namely the right one, produces a distinct wake that is separated from that of the skater's back. Finally, significant velocity deficit is encountered also behind the head (Z = 1 m & Y = 0.1 m), which is not seen in the wake of the other posture.

Puelles Magan et al. (2021) reported the presence of a counter-rotating streamwise vortex pair in the wake of a skater. This characteristic vortex pair is also visible in Fig. 12 for both postures. When both arms are on the back, this vortex pair is located at the height of the lower back (Z = 0.8 m), whereas when only one arm is on the back, the vortex pair induces a downwash and hence, is convected downwards (Z = 0.5 m). Furthermore, it has to be noted that, for the case where only one arm is on the back, a second counter-rotating vortex pair is originated behind the head (Z = 1 m & X = 0.1 m), resulting in a significant upwash trend.

### 4.4. Flow visualizations for skater B (Case 2): low trunk vs. high trunk

Similar to the discussion of case 1 in the previous section, the average velocity and vorticity fields measured 0.5 m behind the lower back of the skater for both configurations in case 2 are shown in Figs. 13 and 14, respectively. For both configurations, the average is obtained from 3 passages where the skater is in phase 2 with the left skate out and the right arm loose from the body.

The near wake of the two configurations clearly exhibit similar streamwise velocity contours; nevertheless, the wake of the low trunk posture has a smaller vertical extensions. In both configurations, the strongest velocity deficit occurs behind the trunk and upper legs, while the wake extends also behind the loose (right) arm and (left) leg. Overall, the wake of the high trunk posture exhibits higher velocity deficits compared to the wake of the low trunk posture.

The vorticity contours of Fig. 14 show that the same main counter-rotating streamwise vortex pair behind the lower back and upper legs is present for both configurations. Similar to the configuration with one arm loose discussed in section 4.3, there is a strong in-wash flow over the extended (left) leg, which corresponds to the side where the arm is attached to the body; such in-wash induces a motion of the vortex pair
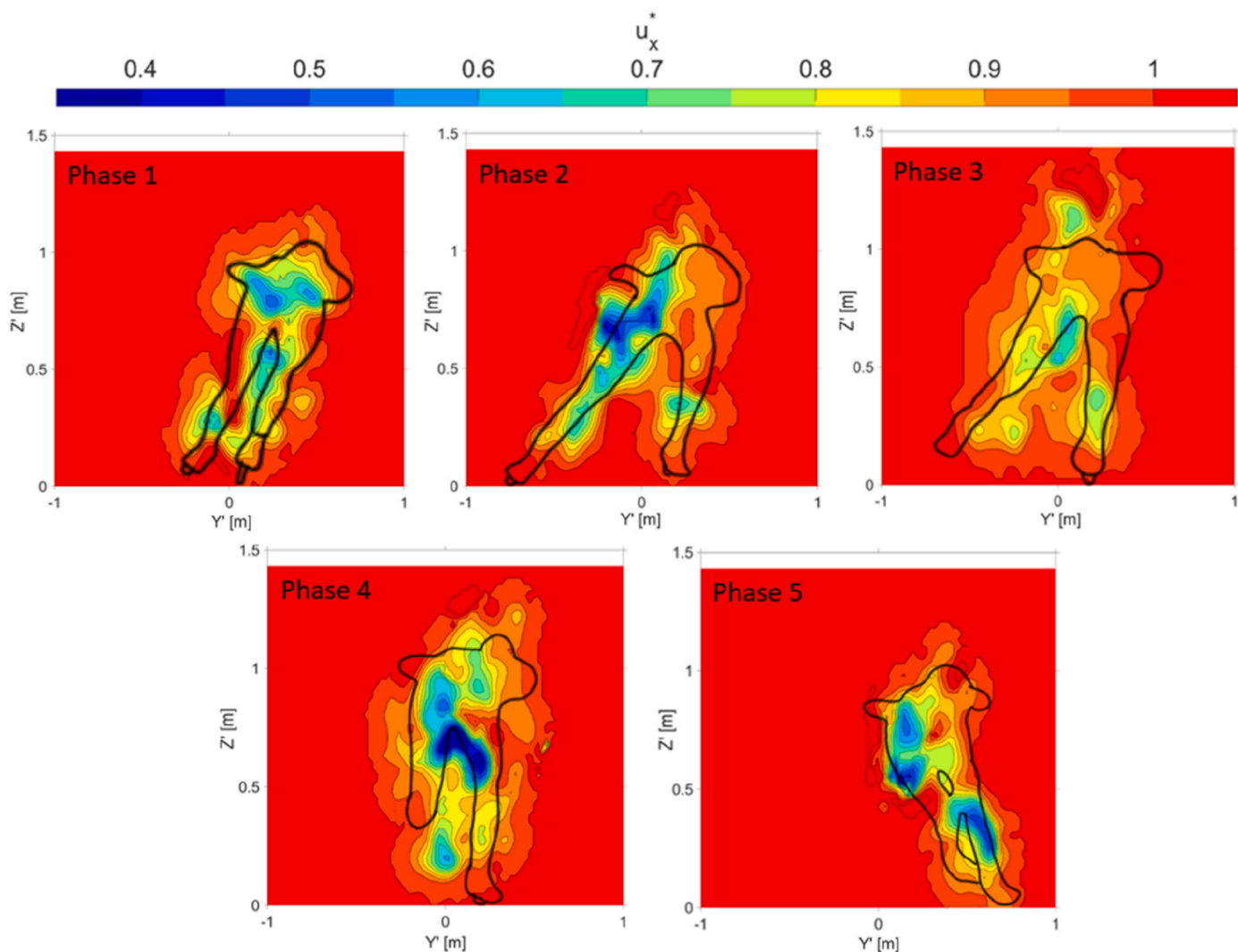
Fig. 10. Instantaneous streamwise velocity u_x^* at X = 0.5 m for skater A with both arms on the back corresponding to the different skating phases as described by van der Kruk et al. (2018). The skater contours are meant as an indication of the location of the skater with respect to their wake and do not reproduce the exact location of the skater.
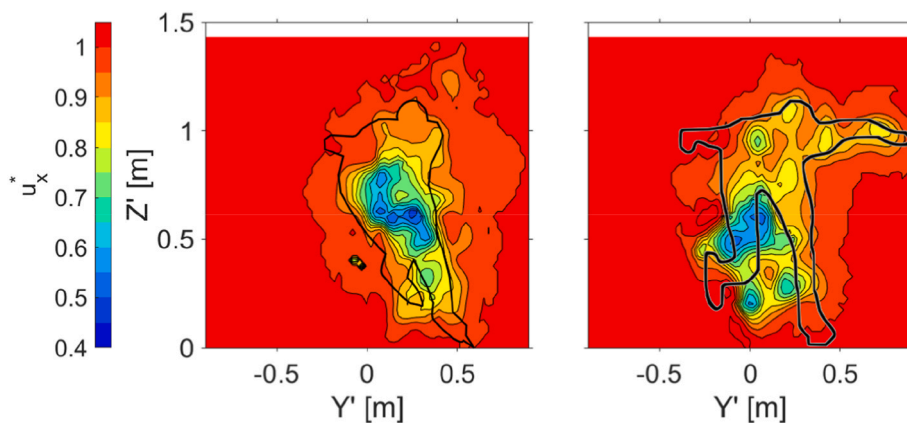
Fig. 11. Average streamwise velocity u_x^* at X = 0.5 m for the skater with both arms on the back in phase 4 (left), and with only one arm on the back in phase 4 (right). Average obtained from two runs.

towards the bent leg (from top-left towards downward-right). Furthermore, the second counter-rotating vortex pair originating from the head (Z = 0.8 m & Y = 0.4 m) is visible for both high- and low-trunk configurations. However, contrary to the upwash trend discussed in Fig. 12-right for case 1, here the vortex pair produces a slight downwash. The latter result is attributed to the swing motion of the right arm: in
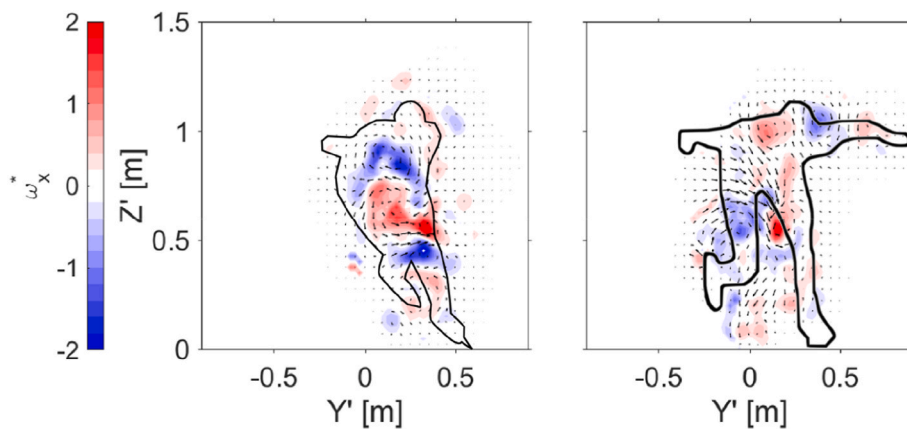
Fig. 12. Average vorticity ω_x^* at X = 0.5 m for the skater with both arms on the back in phase 4 (left), and with only one arm on the back in phase 4 (right). Average obtained from two runs.
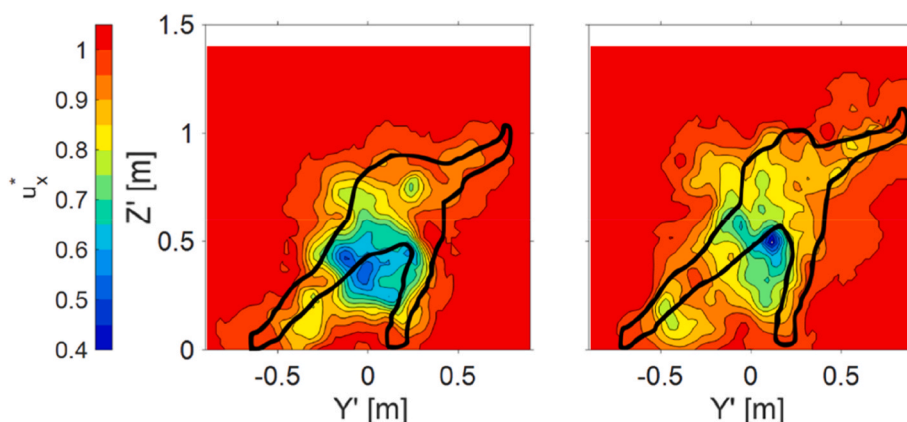

Fig. 13. Average streamwise velocity u_x^* at X = 0.5 m for the skater in low trunk posture in phase 2 (left), and in high trunk posture in phase 2 (right). Average obtained from three runs.
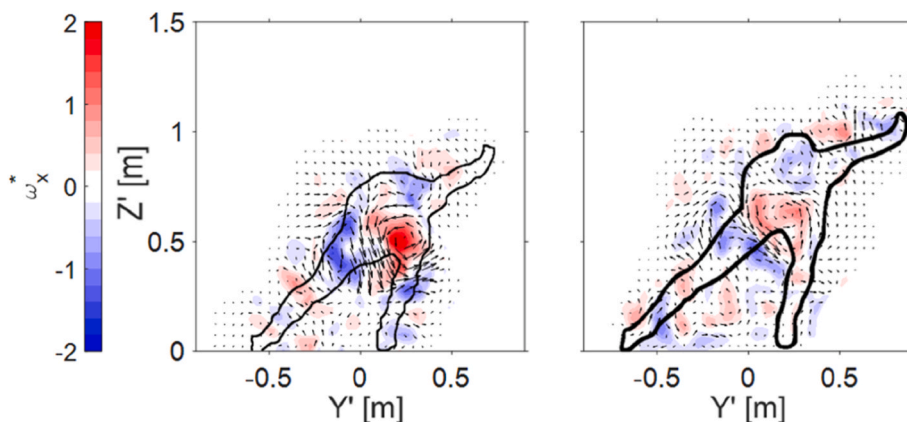

Fig. 14. Average vorticity ω_x^* at X = 0.5 m for the skater in low trunk posture in phase 2 (left), in high trunk posture in phase 2 (right). Average obtained from three runs.

case 1, the arm is almost horizontal and moving downward, whereas in both configurations of case 2 the arm is pointing upwards at 45° and is moving upwards. These swing motions cause a downwards and upwards flow behind the arm, respectively, thus resulting in a downwash and an upwash, respectively, between the head and the arm.

4.5. Drag analysis

Figs. 15 and 16 show the evolution of the drag area C_dA at different streamwise distances from the skaters, for the skating configurations 1 and 2, respectively. The development of the C_dA for each passage is presented separately in grey. The spread of these values provides insight into the repeatability of the measurements and thus, among other things, also into how well the skater could repeat their posture over
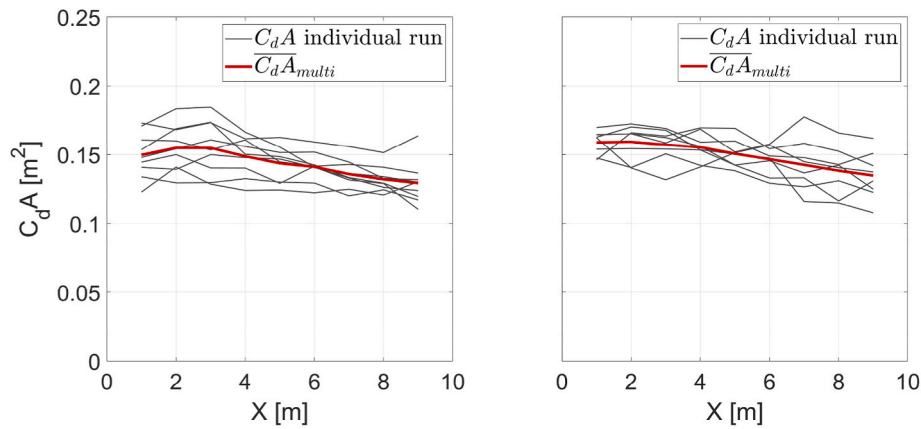
Fig. 15. Evolution of the drag area C_dA at increasing streamwise distances from the skater for the cases with both arms on the back (left) and with only one arm on the back (right).
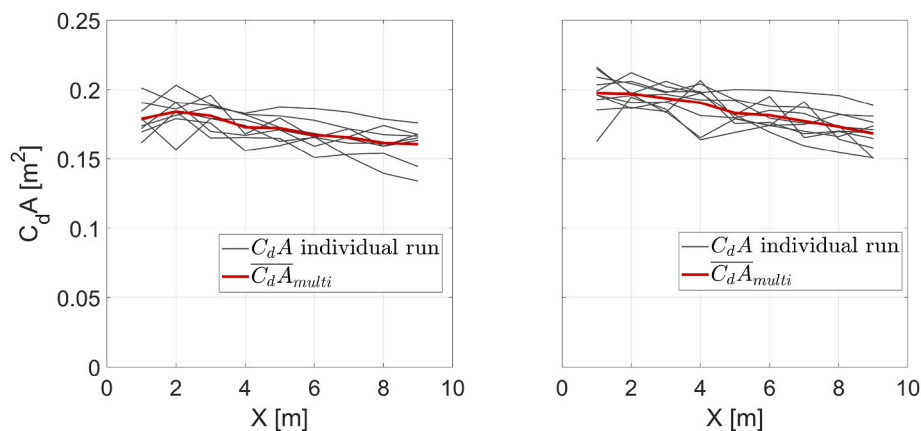

Fig. 16. Evolution of the drag area C_dA at increasing streamwise distances from the skater for the cases of low trunk posture (left) and high trunk posture (right).

multiple runs. Furthermore, the average drag area among multiple passages $\overline{C_dA}_{multi}$ is plotted in red in the figures. Instantaneous information on the wake development at increasing distance from the skater in two different skating phases is presented in a related publication from the authors (Terra et al., 2023).

For case 1 (Fig. 15), it is observed that the drag areas vary by about 0.02 m^2 among different passages; this variation is attributed to the slightly different postures of the skaters when skating with the two arms in the back. After inspection of the raw images, it was found that the larger spread was caused by the fact that for the 'two arms on back' posture the skater passed the measurement region at different skating phases, whereas for the 'one arm on the back' posture the skater was able to pass every run more or less in the same skating phase. This finding indicates that the aerodynamic drag varies during the skating motion. However, the variation of the aerodynamic drag with different skating phases is beyond the scope of this work and thus left to future investigations. Additionally, it is noticed that the drag areas (both the individual runs and the ensemble average) decrease slightly with time (viz. the distance from the skater). The latter result is due to the interaction between the athletes' wakes and the ground, which causes a loss of momentum and thus results in a lower measured momentum deficit. For the two postures of one arm on the back or two arms on the back (Fig. 15 left and right), the ensemble-average drag areas show little differences and attain values of around 0.15 m^2.

In Fig. 16, the drag area evolution for case 2 (low vs high trunk angles) is presented. In this case, the spread of the drag areas among the different runs is smaller than that for case 1 (one vs two arms on the back), indicating higher repeatability of the measurements.

Furthermore, the difference in the ensemble-average drag areas $\overline{C_dA}_{multi}$ (red lines) between the two postures is also more visible than in the previous case, with a larger drag area obtained when the skater is skating with a high trunk angle.

The ensemble average drag area $\overline{C_dA}_{ens}$ for the different skating configurations is calculated from the measurements of each individual passage through the Ring of Fire and illustrated in Fig. 17. For the 'two arms on back' posture of case 1 the drag area is found to be 0.144 m^2, with a 95% confidence level uncertainty of ± 0.009 m^2 (6%). Similarly, for the 'one arm on the back' posture the drag area is increased to 0.151 m^2 with an uncertainty of ± 0.008 m^2 at 95% confidence level, corresponding to 5% of the measured value. Instead, for case 2, larger difference in the ensemble average drag area $\overline{C_dA}_{ens}$ are observed: the $\overline{C_dA}_{ens}$ for the high trunk configuration is 0.185 m^2, whereas it decreases to 0.172 m^2 for the low trunk configuration. In both configurations, the uncertainty at 95% confidence level is 0.006 m^2, or about 3% of the measured drag area.

In order to determine whether the differences in the ensemble average drag areas ($\overline{C_dA}_{ens}$) for the different configurations are statistically significant, the two-sample *t*-test is employed (Snedecor and Cochran, 1996). For this test to be valid, the data is assumed to be independent and normally distributed; additionally, the variances for the two independent sets of measurements are assumed to be equal. The latter is confirmed by an F-test (Snedecor and Cochran, 1996). The significance level is $\alpha = 0.05$, corresponding to 95% confidence level, and the null hypothesis is $\overline{C_dA}_{ens,1} = \overline{C_dA}_{ens,2}$. In other words, if the p-value is smaller than $\alpha = 0.05$, there is 95% confidence that the
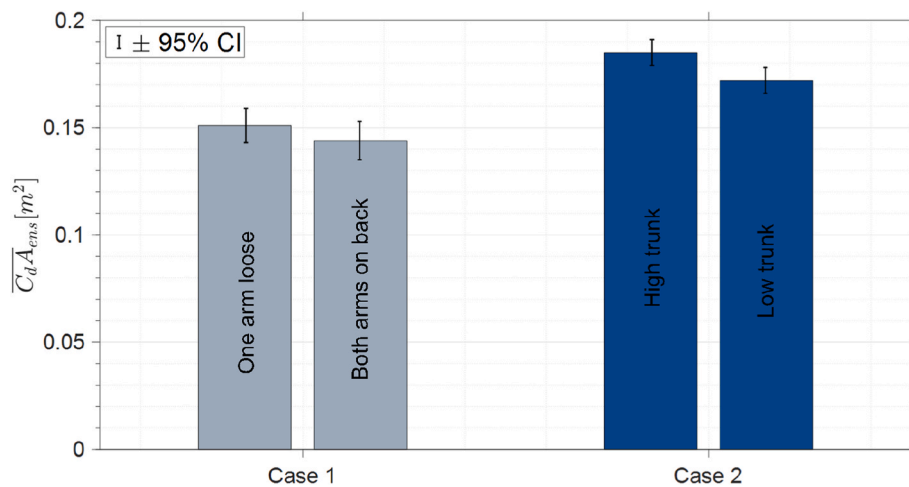
Fig. 17. Comparison between the average drag area $\overline{C_dA}_{ens}$ for the different configurations; uncertainty bars represent the expanded uncertainty at 95% confidence level.

difference between the measured $\overline{C_dA}_{ens}$ values corresponds to an actual difference in drag area between two skating configurations.

The results for the two-sided, two-sample t-test are presented in Table 2. The t-statistics for case 1 and 2 are 1.36 and 3.57, yielding p-values of 0.194 and 0.002, respectively. It is recalled that, when a p-value is less than or equal to the significance level α, the null hypothesis can be rejected, meaning that the measured difference between $\overline{C_dA}_{ens,1}$ and $\overline{C_dA}_{ens,2}$ is statistically significant. For case 1, the p-value is equal to 0.194, which is larger than $\alpha = 0.05$: thus, from the current measurements it is not possible to conclude whether there is an aerodynamic benefit to skating with both arms on the back as compared to skating with only one arm on the back. On the other hand, for case 2, the p-value of 0.002 is clearly below the significance level: hence, it can be concluded that skating in the low trunk posture will provide the skater with a significant aerodynamic benefit.

5. Conclusions

We conducted large-scale stereo-PIV measurements to investigate the flow field in the wake of speed skaters in motion and to determine their aerodynamic drag. A dedicated measurement setup called Ring of Fire was built on the 400 m track at Thialf in Heerenveen. The athletes were skating through the Ring of Fire at a nominal velocity of 11 m/s; for each run, the flow velocity was measured before and after the passage of the skaters. Four different skating configurations have been analysed with two different athletes. For the first athlete, the position of the arms was varied between both arms on the back and one arm swinging loose next to the body. The second athlete was swinging both arms loose for all the runs, but was varying his trunk angle between a low-trunk and a high-trunk configuration.

For all the postures, average streamwise velocity and vorticity fields were presented. In all cases, the maximum velocity deficit in the wake was in the range of $0.45 \leq u_x^* \leq 0.55$ and was located behind the lower back and upper legs. Furthermore, the characteristic vortex pair in the wake of the skater, reported in the literature, was also seen here for all different test cases, indicating that it is independent of the athlete, posture, and skating phase. Finally, a second vortex pair was found behind the skater's head when at least one arm is loose from the body.

The ensemble average aerodynamic drag was evaluated via a control volume approach along the wake behind the skater, accounting for the non-uniform flow conditions prior to the skater's passage. The uncertainty of the average drag measurements from the RoF was about 5%. To evaluate whether the differences between the mean drag areas were statistically significant, a two-sample t-test was performed. In our

Table 2
Two sample t-test parameters for both cases.

Configuration	Case 1		Case 2	
	One arm loose	Both arms on back	High trunk	Low trunk
Mean $\overline{C_dA}_{ens}$ [m^2]	0.151	0.144	0.185	0.172
Standard deviation [m^2]	0.009	0.012	0.008	0.008
Number of samples	8	9	10	9
Degrees of freedom (DF)	15		17	
t-statistic	1.36		3.57	
p-value	0.194		0.002	
Null hypothesis rejected (difference statistically significant)	**No**		**Yes**	

measurements, the difference in drag area between skating with both your arms on the back or with just one arm on the back was found to be not statistically significant. Instead, skating with low trunk angle resulted in a statistically significant drag reduction by 7.5% compared to skating with high trunk angle.

CRediT authorship contribution statement

Alexander Spoelstra: Data curation, Formal analysis, Investigation, Software, Visualization, Writing – original draft. **Wouter Terra:** Conceptualization, Data curation, Investigation, Methodology, Project administration, Resources, Supervision, Validation, Visualization, Writing – review & editing. **Andrea Sciacchitano:** Conceptualization, Funding acquisition, Investigation, Project administration, Resources, Supervision, Validation, Writing – review & editing.

Declaration of competing interest

The authors declare that they have no known competing financial interests or personal relationships that could have appeared to influence the work reported in this paper.

Data availability

Data will be made available on request.

References

Broker, J.P., Kyle, C.R., Burke, E.R., 1999. Racing cyclist power requirements in the 4000-m individual and team pursuits. Med. Sci. Sports Exerc. 31 (11), 1677–1685. https://doi.org/10.1097/00005768-199911000-00026.

Brownlie, L.W., Kyle, C.R., 2012. Evidence that skin suits affect long track speed skating performance. Procedia Eng. 34, 26–31.

Chowdhury, H., Naito, K., Alam, F., 2015. An experimental study on speed skating skinsuits. Mech. Eng. Res. J. 9, 110–114.

Crouch, T.N., Burton, D., Brown, N.A.T., Thompson, M.C., Sheridan, J., 2014. Flow topology in the wake of a cyclist and its effect on aerodynamic drag. J. Fluid Mech. 748, 5–35. https://doi.org/10.1017/jfm.2013.678.

D'Auteuil, A., Larose, G.L., Zan, S.J., 2012. Wind turbulence in speed skating: measurement, simulation and its effect on aerodynamic drag. J. Wind Eng. Ind. Aerod. 104–106, 585–593. https://doi.org/10.1016/j.jweia.2012.02.002.

MYLAPS, 2021. ProChip system. Retrieved from. https://www.mylaps.com/timing-solutions-active-prochip/?noredirect=en_US.

Oggiano, L., Sætran, L., 2008. Effect of different skin suits on speed skating performances. Comput. Sci. Sports 3, 139–144.

Oggiano, L., Sætran, L.R., 2010. Experimental analysis on parameters affecting drag force on speed skaters. Sports Technol. 3 (4), 223–234. https://doi.org/10.1080/19346182.2012.663532.

Puelles Magán, G., Terra, W., Sciacchitano, A., 2021. Aerodynamics Analysis of Speed Skating Helmets: Investigation by CFD Simulations, vol. 11, p. 3148, 7.

Scarano, F., Ghaemi, S., Caridi, G.C.A., Bosbach, J., Dierksheide, U., Sciacchitano, A., 2015. On the use of helium-filled soap bubbles for large-scale tomographic PIV in wind tunnel experiments. Exp. Fluid 56 (2), 42. https://doi.org/10.1007/s00348-015-1909-7.

Sciacchitano, A., Wieneke, B., 2016. PIV uncertainty propagation. Meas. Sci. Technol. 27 (8), 084006.

Snedecor, G.W., Cochran, W.G., 1996. Statistical Methods, 8 ed. Iowa State Univ. Press, Ames, Iowa. 7.

Spoelstra, A., de Martino Norante, L., Terra, W., Sciacchitano, A., Scarano, F., 2019. On-site cycling drag analysis with the Ring of Fire. Exp. Fluid 60 (6), 90. https://doi.org/10.1007/s00348-019-2737-y.

Spoelstra, A., Hirsch, M., Sciacchitano, A., Scarano, F., 2020. Uncertainty Assessment of the Ring of Fire Concept for On-Site Aerodynamic Drag Evaluation. Measurement Science and Technology.

Terra, W., Sciacchitano, A., Scarano, F., 2017. Aerodynamic drag of a transiting sphere by large-scale tomographic-PIV. Exp. Fluid 58, 1–14.

Terra, W., Sciacchitano, A., Scarano, F., van Oudheusden, B.W., 2018. Drag resolution of a PIV wake rake for transiting models. Exp. Fluids 59, 1–6.

Terra, W., Spoelstra, A., Sciacchitano, A., 2023. Aerodynamic benefits of drafting in speed skating: estimates from in-field skater's wakes and wind tunnel measurements. J. Wind Eng. Ind. Aerod. 233, 105329.

Thialf, 2021. Ijsfaciliteiten. Retrieved from. https://thialf.nl/thialf/ijsfaciliteiten.

Timmer, N., Veldhuis, L., 2021. The Impact of Skinsuit Zigzag Tape Turbulators on Speed Skating Performance. 11(3), p. 988.

Van der Kruk, E., 2018. Parameter Analysis for Speed Skating Performance (PhD Thesis). TU Delft.

van der Kruk, E., Schwab, A.L., van der Helm, F.C.T., Veeger, H.E.J., 2018. Getting in shape: reconstructing three-dimensional long-track speed skating kinematics by comparing several body pose reconstruction techniques. J. Biomech. 69, 103–112. https://doi.org/10.1016/j.jbiomech.2018.01.002.

van Ingen Schenau, G.J., 1982. The influence of air friction in speed skating. J. Biomech. 15 (6), 449–458. https://doi.org/10.1016/0021-9290(82)90081-1.

van Oudheusden, B.W., 2013. PIV-based pressure measurement. Meas. Sci. Technol. 24 (3), 032001 https://doi.org/10.1088/0957-0233/24/3/032001.